The Astronomical Journal, 159:160 (12pp), 2020 April https://doi.org/10.3847/1538-3881/ab775a

LHS 1815b: The First Thick-disk Planet Detected by *TESS*

Tianjun Gan[1], Avi Shporer[2], John H. Livingston[3], Karen A. Collins[4], Shude Mao[1,5], Alessandro A. Trani[3], Davide Gandolfi[6], Teruyuki Hirano[7], Rafael Luque[8,9], Keivan G. Stassun[10,11], Carl Ziegler[12], Steve B. Howell[13], Coel Hellier[14], Jonathan M. Irwin[4], Jennifer G. Winters[4], David R. Anderson[14,15], César Briceño[16], Nicholas Law[17], Andrew W. Mann[17], Xavier Bonfils[18], Nicola Astudillo-Defru[19], Eric L. N. Jensen[20], Guillem Anglada-Escudé[21], George R. Ricker[2], Roland Vanderspek[2], David W. Latham[22], Sara Seager[2,23,24], Joshua N. Winn[25], Jon M. Jenkins[13], Gabor Furesz[2], Natalia M. Guerrero[2], Elisa Quintana[26], Joseph D. Twicken[13,27], Douglas A. Caldwell[13,27], Peter Tenenbaum[13,27], Chelsea X. Huang[2,30], Pamela Rowden[28], and Bárbara Rojas-Ayala[29]
[1] Department of Astronomy and Tsinghua Centre for Astrophysics, Tsinghua University, Beijing 100084, People's Republic of China; gtj18@mails.tsinghua.edu.cn
[2] Department of Physics and Kavli Institute for Astrophysics and Space Research, Massachusetts Institute of Technology, Cambridge, MA 02139, USA
[3] Department of Astronomy, The University of Tokyo, 7-3-1 Hongo, Bunkyo-ku, Tokyo 113-0033, Japan
[4] Center for Astrophysics | Harvard & Smithsonian, 60 Garden Street, Cambridge, MA 02138, USA
[5] National Astronomical Observatories, Chinese Academy of Sciences, 20A Datun Road, Chaoyang District, Beijing 100012, People's Republic of China
[6] Dipartimento di Fisica, Università degli Studi di Torino, via Pietro Giuria 1, I-10125, Torino, Italy
[7] Department of Earth and Planetary Sciences, Tokyo Institute of Technology, 2-12-1 Ookayama, Meguro-ku, Tokyo 152-8551, Japan
[8] Instituto de Astrofísica de Canarias (IAC), E-38205 La Laguna, Tenerife, Spain
[9] Departamento de Astrofísica, Universidad de La Laguna (ULL), E-38206, La Laguna, Tenerife, Spain
[10] Department of Physics and Astronomy, Vanderbilt University, 6301 Stevenson Center Ln., Nashville, TN 37235, USA
[11] Department of Physics, Fisk University, 1000 17th Avenue North, Nashville, TN 37208, USA
[12] Dunlap Institute for Astronomy and Astrophysics, University of Toronto, 50 St. George Street, Toronto, Ontario M5S 3H4, Canada
[13] NASA Ames Research Center, Moffett Field, CA 94035, USA
[14] Astrophysics Group, Keele University, Staffordshire, ST5 5BG, UK
[15] Centre for Exoplanets and Habitability, University of Warwick, Gibbet Hill Road, Coventry CV4 7AL, UK
[16] Cerro Tololo Inter-American Observatory, Casilla 603, La Serena, Chile
[17] Department of Physics and Astronomy, The University of North Carolina at Chapel Hill, Chapel Hill, NC 27599-3255, USA
[18] Univ. Grenoble Alpes, CNRS, IPAG, F-38000 Grenoble, France
[19] Departamento de Matemática y Física Aplicadas, Universidad Católica de la Santísima Concepción, Alonso de Rivera 2850, Concepción, Chile
[20] Dept. of Physics & Astronomy, Swarthmore College, Swarthmore PA 19081, USA
[21] School of Physics and Astronomy, Queen Mary University of London, 327 Mile End Road, London, E1 4NS, UK
[22] Harvard-Smithsonian Center for Astrophysics, 60 Garden Street, Cambridge, MA 02138, USA
[23] Department of Earth, Atmospheric and Planetary Sciences, Massachusetts Institute of Technology, Cambridge, MA 02139, USA
[24] Department of Aeronautics and Astronautics, MIT, 77 Massachusetts Avenue, Cambridge, MA 02139, USA
[25] Department of Astrophysical Sciences, Princeton University, 4 Ivy Lane, Princeton, NJ 08544, USA
[26] NASA Goddard Space Flight Center, 8800 Greenbelt Road, Greenbelt, MD 20771, USA
[27] SETI Institute, Mountain View, CA 94043, USA
[28] School of Physical Sciences, The Open University, Milton Keynes MK7 6AA, UK
[29] Instituto de Alta Investigación, Universidad de Tarapacá, Casilla 7D, Arica, Chile
Received 2019 December 22; revised 2020 February 13; accepted 2020 February 16; published 2020 March 18

Abstract

We report the first discovery of a thick-disk planet, LHS 1815b (TOI-704b, TIC 260004324), detected in the *Transiting Exoplanet Survey Satellite* (*TESS*) survey. LHS 1815b transits a bright ($V = 12.19$ mag, $K = 7.99$ mag) and quiet M dwarf located 29.87 ± 0.02 pc away with a mass of $0.502 \pm 0.015\,M_{\odot}$ and a radius of $0.501 \pm 0.030\,R_{\odot}$. We validate the planet by combining space- and ground-based photometry, spectroscopy, and imaging. The planet has a radius of $1.088 \pm 0.064\,R_{\oplus}$ with a 3σ mass upper limit of $8.7\,M_{\oplus}$. We analyze the galactic kinematics and orbit of the host star LHS 1815 and find that it has a large probability ($P_{\rm thick}/P_{\rm thin} = 6482$) to be in the thick disk with a much higher expected maximal height ($Z_{\rm max} = 1.8$ kpc) above the Galactic plane compared with other *TESS* planet host stars. Future studies of the interior structure and atmospheric properties of planets in such systems using, for example, the upcoming *James Webb Space Telescope*, can investigate the differences in formation efficiency and evolution for planetary systems between different Galactic components (thick disks, thin disks, and halo).

Unified Astronomy Thesaurus concepts: Astrometric exoplanet detection (2130); Astrometry (80); Stellar kinematics (1608); Transit photometry (1709); Radial velocity (1332)

1. Introduction

Since Gilmore & Reid (1983) first proposed subdivision between the thick disk and thin disk after studying the stellar luminosity function and Galactic stellar number density gradient, the study of the origin of Galactic disks has been a hot topic over the past few decades. Current theories postulate that the Milky Way (MW) is made up of several components: a thin disk, a thick disk, a halo and a bulge. Further studies indicate that solar neighborhood stars are mostly members of the Galactic disk, with a small fraction belonging to the halo (Buser et al. 1999; Jurić et al. 2008; Bensby et al. 2014). In general, compared with thin-disk stars, stars in the thick disk are older (Bensby et al. 2005; Fuhrmann 2008; Adibekyan et al. 2011), and have enhanced α-elements abundance and lower metallicity (Prochaska et al. 2000;

[30] Juan Carlos Torres Fellow.

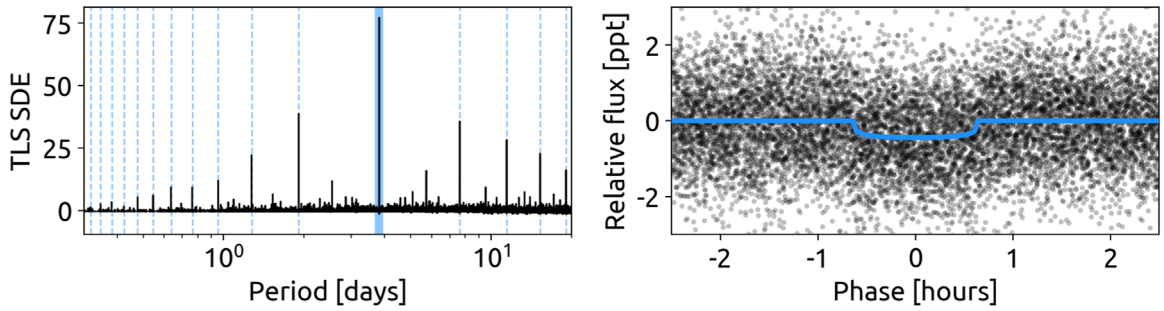

Figure 1. Left: TLS power spectrum of the *TESS* photometry of LHS 1815, with the detected orbital period indicated by a blue shaded region, as well as harmonics and subharmonics indicated by blue dotted lines. Right: *TESS* photometry phase-folded on the detected orbital period, with the TLS transit model in blue; this model was subtracted from the data to search for additional transit signals, but none were found.

Reddy et al. 2006; Adibekyan et al. 2013) as well as hotter kinematic features (Adibekyan et al. 2013; Bensby et al. 2014), which could affect the planet formation efficiency (Gonzalez 1997; Neves et al. 2009).

To date, more than 4000 exoplanets[31] have been detected, thanks to successful surveys such as HATNet (Bakos et al. 2004), SuperWASP (Pollacco et al. 2006), and space-based missions including *CoRoT* (Baglin et al. 2006), *Kepler* (Borucki et al. 2010), and K2 (Howell et al. 2014). However, few of the known exoplanets have been claimed to show thick-disk features (Reid et al. 2007; Fuhrmann & Bernkopf 2008; Neves et al. 2009; Bouchy et al. 2010; Campante et al. 2015). The difference in planet formation and evolution between the thick and thin disks of the MW is still a mystery. Interestingly, a recent work from McTier & Kipping (2019) implies that planets in the solar neighborhood are just as likely to form around fast-moving stars (thick-disk) as they are around slow-moving stars (thin-disk). Because a common way to separate different components of the MW relies on the spatial motion of stars, potential large biases may arise from radial velocity (RV) measurement limits as the RV survey of *Gaia* DR2 focuses on relatively bright stars ($G \lesssim 16.2$ mag). Only ∼150 million stars have RV measurements (Sartoretti et al. 2018), so kinematic information of most faint stars is still lacking.

The successful launch of the *Transiting Exoplanet Survey Satellite* (*TESS*; Ricker et al. 2014) opened a new era in this area, aiming at detecting small exoplanets around bright stars, and capable of discovering about $\sim 10^4$ planets during its primary mission (Sullivan et al. 2015; Huang et al. 2018b). The *TESS* survey can provide a large sample of solar neighborhood transiting planets across the whole sky. All planet host stars are bright enough to have their RV measured by the *Gaia* survey. It will be an excellent opportunity to study the difference in the planet evolution between the thin and thick disks.

Here, we present the discovery of LHS 1815b, an Earth-size planet on a short 3.1843 day orbit, transiting a nearby M1-type dwarf. It is the first planetary system detected in the Galactic thick disk during the two-year survey of *TESS*.

This paper is organized as follows: In Section 2, we describe the space and ground-based observations. Section 3 presents the analysis about the stellar characterization of LHS 1815 along with results of the joint fit. We focus on the tidal evolution in Section 4. In Section 5, we discuss the thick-disk features of LHS 1815. We conclude our findings in Section 6.

[31] https://exoplanetarchive.ipac.caltech.edu/

2. Observations

2.1. TESS

LHS 1815 (TIC 260004324) falls in *TESS*'s continuous viewing zone and it was observed with the two-minute cadence mode, spanning from 2018 July 25th to 2019 July 17th. Data ranges from Sector 1 to Sector 13 while excluding Sector 6, and it consists of a total of 229,712 exposures.

Once images were transmitted to Earth, they were reduced by using the Science Processing Operations Center (SPOC) pipeline (Jenkins et al. 2016), which was developed at NASA Ames Research Center based on *Kepler* mission's science pipeline. Transit planet search (Jenkins 2002; Jenkins et al. 2017) was performed to look for transit signals and finally LHS 1815 was alerted on the MIT *TESS* Alerts portal[32] as a planet candidate, designated *TESS* object of interest (TOI) 704.01, with a period of 3.814 days, a transit depth of ∼400 ppm, and a transit duration of ∼1.4 hr.

We downloaded photometric data from the Mikulski Archive for Space Telescopes (MAST[33]) and used the two-minute Presearch Data Conditioning Simple Aperture Photometry light curve from the SPOC pipeline for our transit analyses (Smith et al. 2012; Stumpe et al. 2012, 2014), which has been corrected for instrumental and systematic effects. To improve the precision of the light curve, we ignored data where the SPOC quality flag was nonzero. We performed the detrending by fitting a spline model to the raw light curve after masking out all transits (knots spaced every 0.5 days). We divided the light curve by the best-fit spline for normalization.

To independently confirm the 3.814 day signal using all available *TESS* data (12 Sectors), we used the transit least-squares algorithm (TLS; Hippke & Heller 2019) to search the light curve for transits. TLS uses a physically realistic model accounting for limb-darkening and nonzero ingress/egress duration, enabling it to detect shallower transits than box-fitting least squares (BLS). We recovered the 3.814 day transits with a signal detection efficiency (SDE) of ∼75, and subtracted the TLS model from the data to search for additional planets (see Figure 1); several peaks with SDE moderately higher than 15 can be seen in the TLS power spectrum of the residuals, but they all appeared to be caused by noise. We concluded that no other significant transit signals exist in the *TESS* data besides the 3.814 day signal.

[32] https://tess.mit.edu/alerts/
[33] http://archive.stsci.edu/tess/

Table 1
Summary of Photometric Observations for LHS 1815

Facility	Date	Exposure time(s)	Total exposures	Filter	Summary
LCO 1 m SSO Sinistro	2019 Aug 24	130	46	r'	Full
LCO 1 m CTIO Sinistro	2019 Sep 1	70	92	r'	Ingress

2.2. Ground-based Photometry

Though *TESS* has high photometric precision, due to its large pixel scale (21″ per pixel, Ricker et al. 2014), light from nearby stars is blended with the target. Nearby eclipsing binary (NEB) are a common source of false positives in *TESS* (Brown 2003; Sullivan et al. 2015) as they can cause transit-like signals on the target. Ground-based observations have two main goals: one is to reproduce the transit signal, the other is to look for nearby eclipsing binaries and check whether the signal is on the target (Deeg et al. 2009).

In addition to *TESS* photometry, we also acquired two ground-based follow-up observations through 1 m telescopes of the Las Cumbres Observatory Global Telescope Network (LCO)[34] (Brown et al. 2013), summarized in Table 1. We used the Sinistro cameras, which deliver a field of view (FoV) of $26' \times 26'$ with a plate scale of 0.″389 per pixel. Data calibration was done by LCO's automatic BANZAI pipeline. Aperture photometry is performed by using AstroImageJ (Collins et al. 2017).

A full transit of LHS 1815b was observed in the Sloan r' band on 2019 August 24th at Siding Spring Observatory (SSO), Australia. The observation was obtained with 130 s exposure time, aiming to rule out all potential faint nearby eclipsing binaries that may result in the *TESS* detection. We initially aimed at ruling out nearby EBs since the shallow transit depth (400 ppm) is challenging for ground telescopes to detect. Another similar egress observation in r' but with 70 s exposure time was done two orbital periods later at Cerro Tololo Inter-American Observatory (CTIO), Chile. In these observations, we have examined all nearby stars within 2.′5 from the target with brightness difference down to $\Delta T \sim 8.7$ mag identified by *Gaia*[35] (See Figure 2). None of them showed variability (an eclipse) at an amplitude that could have led to the transit seen in *TESS* data when their light is blended with the target on *TESS* CCD.

2.3. High-resolution Spectroscopy

Twenty-two spectra of LHS 1815 were collected with the High Accuracy Radial velocity Planet Searcher (HARPS; Mayor et al. 2003) on the ESO 3.6 m telescope at La Silla Observatory in Chile. The spectrograph has a resolving power of $R \approx 115{,}000$ and covers the spectral range from 380 to 690 nm. These spectra were taken between UT 2003 December 15 and UT 2010 December 18 and are publicly available on the ESO Science Archive Facility.[36] We note that some of the RVs from those spectra were derived using the K5 template and the others with the M2 template.

Here, we used the Template Enhanced Radial velocity Re-analysis Application (TERRA; Anglada-Escudé & Butler 2012) software to homogeneously extract the Doppler measurements from the archival HARPS spectra. TERRA is considered to be more precise for M-dwarfs relative to the HARPS Data Reduction Software (DRS; Perger et al. 2017) whose results are on the HARPS archive. Table 2 lists the HARPS-TERRA RVs and their uncertainties. Time stamps are given in barycentric Julian Date in the barycentric dynamical time ($\mathrm{BJD}_{\mathrm{TDB}}$).

We searched the HARPS-TERRA RVs for the Doppler reflex motion induced by the transiting planet. Figure 3 displays the generalized Lomb–Scargle periodogram (Zechmeister & Kürster 2009) of the HARPS-TERRA RVs within the frequency range 0.0–0.5 day^{-1}. The periodogram has its highest peak at the orbital frequency of the transiting planet ($f_{\mathrm{orb}} = 0.262\ \mathrm{day}^{-1}$). We assessed its false-alarm probability (FAP) following the bootstrap method described in Murdoch et al. (1993). Briefly, we defined the FAP as the probability that the periodogram of fake data sets —obtained by randomly shuffling the Doppler measurements, while keeping their time-stamps fixed—has a peak higher than the peak observed in the periodogram of the HARPS-TERRA RVs. With a false alarm probability of FAP $\approx 30\%$, the signal at $f_{\mathrm{orb}} = 0.262\ \mathrm{day}^{-1}$ is found not to be significant within the frequency range 0.0–0.5 day^{-1}.

However, the *TESS* light curve provides prior knowledge of the possible presence of a Doppler signal at the transiting frequency. We therefore computed the FAP at the orbital frequency of the transiting planet, i.e., the probability that random data sets can produce a peak exactly at $f_{\mathrm{orb}} = 0.262\ \mathrm{day}^{-1}$ and whose power is higher than the power of the peak found in the periodogram of the HAPRS-TERRA RVs. To this aim, we first computed the FAP of 10^5 fake data sets in 11 different spectral ranges centered around $f_{\mathrm{orb}} = 0.262\ \mathrm{day}^{-1}$ and with arbitrary chosen widths[37] of 0.001, 0.041, 0.081, 0.121, 0.161, 0.201, 0.241, 0.281, 0.321, 0.361, and 0.401 day^{-1}. We finally extrapolated the FAP in an infinitesimally narrow window centered around $f_{\mathrm{orb}} = 0.262\ \mathrm{day}^{-1}$ by fitting a quadratic trend to the 11 data points. We found a small false alarm probability of FAP = 0.02%, providing evidence for the existence of a significant Doppler signal at the transiting frequency of the planet.

2.4. High Angular Resolution Imaging

High angular resolution imaging is needed to search for nearby sources that can contaminate the *TESS* photometry, resulting in an underestimated planetary radius, or be the source of astrophysical false positives, such as background eclipsing binaries.

2.4.1. SOAR

We searched for stellar companions to LHS 1815 with speckle imaging on the 4.1 m Southern Astrophysical Research (SOAR) telescope (Tokovinin 2018) on UT 2019 October 16,

[34] https://lco.global/
[35] https://www.astro.louisville.edu/gaia_to_aij/
[36] http://archive.eso.org/wdb/wdb/adp/phase3_spectral/form

[37] We note that the time resolution of the HARPS time-series—defined as the inverse of the time baseline—is 0.0004 day^{-1}, which is 2.5 times lower then the smallest width used in our analysis.

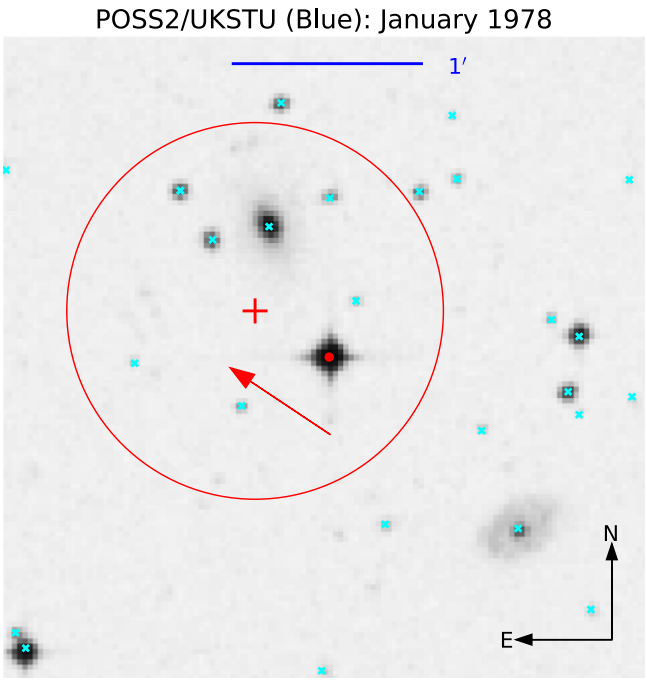

Figure 2. POSS2 blue image of LHS 1815 obtained in 1978. Red point is the location of LHS 1815 in POSS2 while the red cross represents its current position. Red circle indicates a region with a radius of 1′ around LHS 1815. Red arrow indicates the direction of proper motion. Cyan points are stars within 2.′5 retrieved from *Gaia* DR2 that can potentially cause the *TESS* detection, all of which have been cleared by ground-based LCO photometry.

Table 2
HARPS RV Measurements of LHS 1815

BJD_{TDB}	RV ($m\,s^{-1}$)	σ_{RV} ($m\,s^{-1}$)
2452,988.75308	1.30	1.80
2452,998.71510	2.28	2.42
2453,007.72615	0.38	0.81
2453,295.87376	0.94	1.95
2453,834.51235	−4.99	1.43
2454,430.82565	−5.25	1.91
2454,431.76826	0.84	1.62
2454,751.87135	0.00	5.35
2454,803.72204	4.98	4.86
2454,814.73847	−4.50	1.77
2454,833.76771	−6.42	1.73
2454,841.69264	−2.28	1.52
2454,931.50924	3.50	1.53
2455,218.75761	−0.27	1.44
2455,538.64177	5.24	2.22
2455,539.64365	−3.78	1.94
2455,540.66332	−3.39	1.70
2455,542.70589	−0.79	2.28
2455,544.72265	0.36	1.76
2455,546.63073	3.07	2.10
2455,547.74183	−0.79	2.00
2455,548.64140	−1.84	2.29

Note. Time stamps are are given in barycentric Julian Date in the barycentric dynamical time.

observing in a visible bandpass similar to that of *TESS*. The 5σ detection sensitivity and speckle autocorrelation function (ACF) from the observation are shown in Figure 4. No nearby stars were detected in the SOAR observations down to five

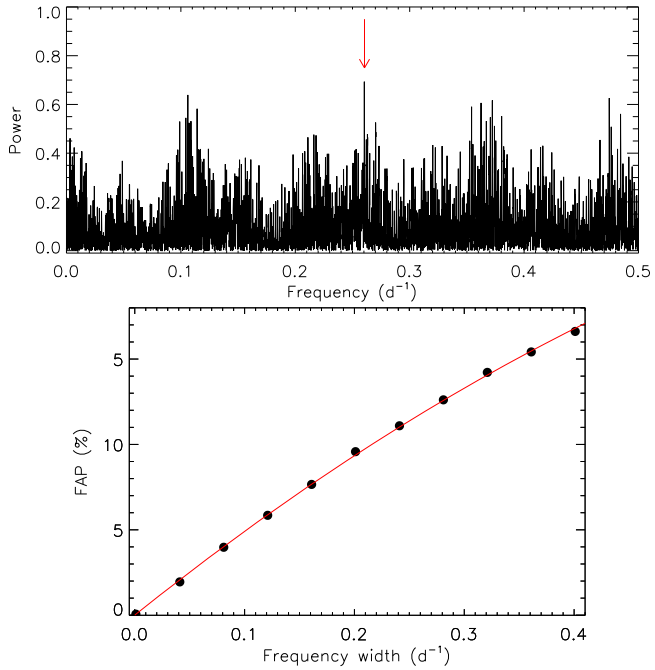

Figure 3. Top: generalized Lomb–Scargle periodogram of the HARPS RVs. Red arrow marks the orbital frequency of the transiting planet ($f_{orb} = 0.262\ day^{-1}$). Bottom: false-alarm probability computed in 11 different spectral ranges centered around the orbital frequency of the transiting planet ($f_{orb} = 0.262\ day^{-1}$) and with a width of 0.001, 0.041, 0.081, 0.121, 0.161, 0.201, 0.241, 0.281, 0.321, 0.361, and 0.401 day^{-1}. Red line marks the best fitting parabolic trend.

magnitudes fainter than the target and as close as 0.″2 to LHS 1815.

2.4.2. Gemini-South

LHS 1815 was also observed on UT 2019 October 8 using the Zorro speckle instrument on Gemini-South.[38] Zorro provides simultaneously high-resolution speckle imaging in two bands, 562 and 832 nm, with output data products including a reconstructed image, and robust limits on companion detections (Howell et al. 2011). Figure 5 shows our results with corresponding reconstructed speckle images from which we find that LHS 1815 is a single star with no companions detected down to a magnitude difference of 5 to 8 mag from the diffraction limit (0.5 au) to 1.″75 (54 au).

3. Analysis

3.1. Stellar Characterization

3.1.1. Empirical Relation

We used Two Micron All Sky Survey (2MASS) m_{K_S} (Cutri et al. 2003; Skrutskie et al. 2006) and the parallax from *Gaia* DR2 (Gaia Collaboration et al. 2018) to calculate the K_S band absolute magnitude $M_{K_S} = 5.62 \pm 0.02$ mag. We estimated the bolometric correction to be 2.61 ± 0.06 mag through the empirical polynomial relation in Mann et al. (2015). We obtained a bolometric magnitude $M_{bol} = 8.23 \pm 0.06$ mag, leading to a luminosity of $L_\star = 0.040 \pm 0.002\,L_\odot$.

To compute the effective temperature T_{eff} of the host star, we applied two different methods. Following the polynomial relation between T_{eff} and $V-J$ in Pecaut & Mamajek (2013), we obtained

[38] https://www.gemini.edu/sciops/instruments/alopeke-zorro/

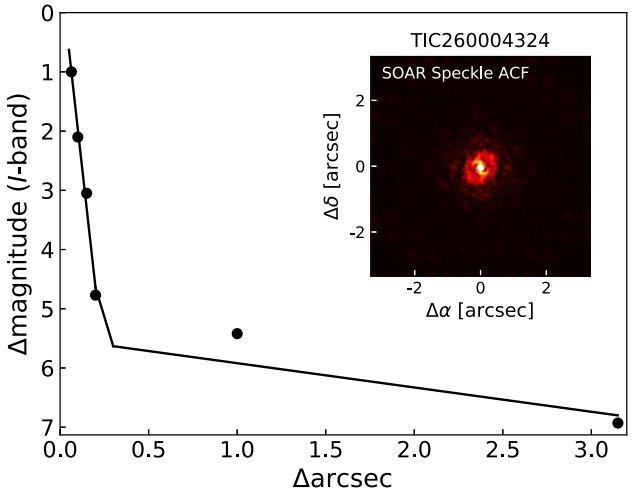

Figure 4. Speckle ACF obtained in the I band using SOAR. The 5σ contrast curve for LHS 1815 is shown by the black points. Black solid line corresponds to the linear fit of the data, at separations smaller and larger than $\sim 0\farcs2$.

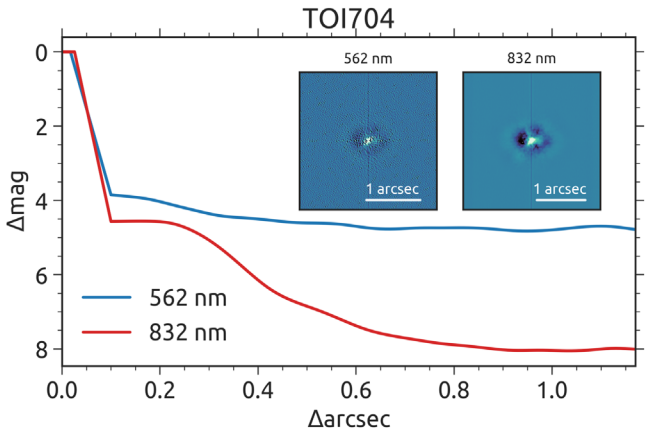

Figure 5. Zorro speckle imaging and 5σ contrast curves of LHS 1815 at 562 and 832 nm. The data reveal that no companion star is detected from the diffraction limit (17 mas) out to $1\farcs75$ within a Δm of 5 to 8.

$T_{\rm eff} = 3658 \pm 103$ K. We also determined $T_{\rm eff}$ based on the Stefan–Boltzmann law. First, we estimated the radius of the host star $0.50 \pm 0.03\,R_\odot$ using the $R_\star - M_{K_S}$ relation in Mann et al. (2015). Next, we derived $T_{\rm eff} = 3630 \pm 98$ K, which agrees well with the result from the first method.

We evaluated the mass of the host star $M_\star = 0.502 \pm 0.015\,M_\odot$ using Equation (2) in Mann et al. (2019) based on the $M_\star - M_{K_S}$ polynomial relation.

3.1.2. Spectroscopic Parameters

Following Hirano et al. (2018), we also used the coadded HARPS spectra signal-to-noise ratio (S/N = 115 at 6000 Å) as input to SpecMatch-Emp (Yee et al. 2017) to derive the stellar effective temperature $T_{\rm eff}$, radius $R_\star$, and iron abundance [Fe/H]. By matching the input spectrum to a high-resolution spectral library of 404 stars, this method yields $T_{\rm eff} = 3553 \pm 70$ K, $R_\star = 0.454 \pm 0.100\,R_\odot$, and [Fe/H] $= -0.12 \pm 0.09$.

3.1.3. SED Analysis

As an independent check on the derived stellar parameters, we performed an analysis of the broadband spectral energy distribution (SED) together with the *Gaia* DR2 parallax in order to determine an empirical measurement of the stellar radius, following the procedures described in Stassun & Torres (2016) and Stassun et al. (2017, 2018a). We gathered the U, B, V magnitudes from Mermilliod (2006), the J, H, K_S magnitudes from 2MASS Point Source Catalog (Cutri et al. 2003; Skrutskie et al. 2006), four *Wide-field Infrared Survey Explorer* (*WISE*) magnitudes (Wright et al. 2010) and three *Gaia* magnitudes G, $G_{\rm BP}$, $G_{\rm RP}$. Together, the available photometry spans the full stellar SED over the wavelength range 0.3–22 μm.

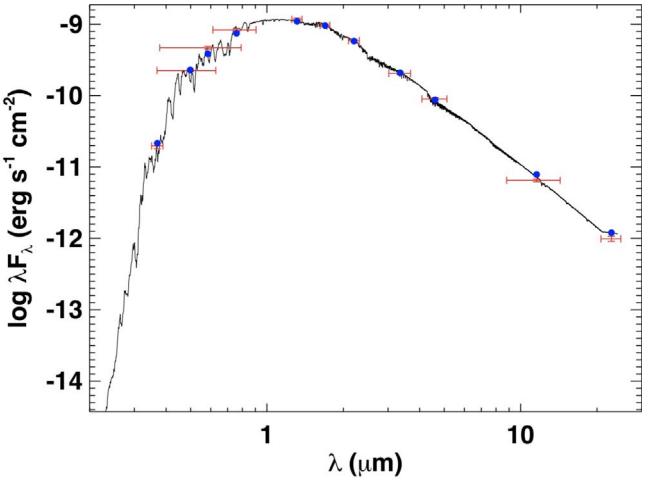

Figure 6. Best SED fit for LHS 1815. Red symbols show the observed photometric measurements, where the horizontal bars represent the effective width of the passband. Blue points are the predicted integrated fluxes at the corresponding bandpass. Black line represents the best-fit NextGen atmosphere model.

We performed a fit using the NextGen stellar atmosphere models, with priors on effective temperature $T_{\rm eff}$ and metallicity ([Fe/H]) from the empirical relations and spectroscopy described above. We set the extinction A_V to zero, due to the proximity of the star. The best-fit SED is shown in Figure 6 with a reduced $\chi^2 = 2.5$, adopting $T_{\rm eff} = 3650 \pm 160$ K and [Fe/H] $= -0.12 \pm 0.09$. Integrating the model SED gives an observed bolometric flux of $F_{\rm bol} = (1.478 \pm 0.070) \times 10^{-9}$ erg s^{-1} cm^{-2}. Taking the $F_{\rm bol}$ and $T_{\rm eff}$ together with the *Gaia* parallax, adjusted by $+0.08$ mas to account for the systematic offset reported by Stassun & Torres (2018), we found a stellar radius of $R = 0.502 \pm 0.044\,R_\odot$, which is consistent with our result based on empirical relations in Section 3.1.1.

Combining all the results above, we adopted the mean values for effective temperature $T_{\rm eff}$ and stellar radius $R_\star$. Together with the expected stellar mass, we found the mean stellar density $\rho_\star = 5.6 \pm 2.7$ g cm^{-3}. We list all stellar parameter values in Table 3.

3.2. Joint Fit

To simultaneously model the transits and RV orbit, we used the EXOplanet traNsits and rAdIaL velocity fittER (EXONAIER; Espinoza et al. 2016). The transit model is created by batman (Kreidberg 2015) while the RV orbit is modeled using radvel (Fulton et al. 2018).

Before we carried out the joint fit, we first created individual fits for *TESS* photometry-only and HARPS RV-only data sets with uniform priors, of which the posteriors are taken into consideration for further joint analysis. For the joint fit, we

Table 3
Basic Stellar Parameters for LHS 1815

Parameter	Value	
Star ID		
2MASS	J06042035-5518468	
Gaia DR2	5500061456275483776	
TIC	260004324	
TOI	704	
LHS	1815	
Equatorial Coordinates		
α (*J*2000)	06:04:20.359	
δ (*J*2000)	−55:18:46.84	
Photometric properties		
TESS (mag)	10.142 ± 0.007	TIC V8[a]
Gaia (mag)	11.236 ± 0.0007	*Gaia* DR2
Gaia BP (mag)	12.407 ± 0.0017	*Gaia* DR2
Gaia RP (mag)	10.180 ± 0.0014	*Gaia* DR2
B_T (mag)	14.027 ± 0.502	Tycho-2
V_T (mag)	12.166 ± 0.202	Tycho-2
B (mag)	13.595 ± 0.011	APASS
V (mag)	12.189 ± 0.03	APASS
J (mag)	8.801 ± 0.024	2MASS
H (mag)	8.209 ± 0.047	2MASS
K_S (mag)	7.993 ± 0.020	2MASS
*WISE*1 (mag)	7.820 ± 0.023	*WISE*
*WISE*2 (mag)	7.736 ± 0.020	*WISE*
*WISE*3 (mag)	7.661 ± 0.016	*WISE*
*WISE*4 (mag)	7.555 ± 0.088	*WISE*
Astrometric properties		
Parallax (mas)	33.48 ± 0.03	*Gaia* DR2
μ_α (mas yr^{-1})	681.73 ± 0.05	*Gaia* DR2
μ_δ (mas yr^{-1})	342.13 ± 0.06	*Gaia* DR2
RV (km s^{-1})	42.22 ± 0.25	*Gaia* DR2
Derived parameters		
Distance (pc)	29.87 ± 0.02	This work
$M_\star$ ($M_\odot$)	0.502 ± 0.015	This work
$R_\star$ ($R_\odot$)	0.501 ± 0.030	This work
$\rho_\star$ (g cm^{-3})	5.6 ± 2.7	This work
log $g_\star$ (cgs)	4.77 ± 0.03	This work
$L_\star$ ($L_\odot$)	0.041 ± 0.004	This work
$T_{\rm eff}$ (K)	3643 ± 142	This work
[Fe/H]	−0.12 ± 0.09	This work
$P_{\rm rot}$ (day)	47.8 ± 0.7	This work

Note.
[a] Stassun et al. (2018b, 2019).

applied uniform priors for planet-to-star radius ratio ($R_P/R_\star$), orbital inclination (i), two quadratic limb-darkening coefficients (q_1 and q_2) with an initial guess taken from Claret (2018), systemic velocity γ, RV semiamplitude (K), and a normal prior for period (P), middle transit time (T_0), and the separation between the host star and the planet in units of the stellar radius ($a/R_\star$) based on the stellar radius and mass (Sozzetti et al. 2007). We applied the Markov chain Monte Carlo (MCMC) analysis to determine the posterior probability distribution of the system parameters using the package emcee (Foreman-Mackey et al. 2013). We first fitted a Keplerian orbit, which gave an eccentricity of 0.4 ± 0.2, indicating the RV data set is insufficient to detect an eccentric orbit. Hence, we assumed a circular orbit and fixed the orbital eccentricity to zero, which is expected given the short orbital period (see Section 4). The posterior of the semiamplitude K is $2.7^{+0.9}_{-1.0}$ m s^{-1}, indicating that the companion of LHS 1815 has a mass 4.2 ± 1.5 $M_\oplus$ with a 3σ upper-limit 8.7 $M_\oplus$. The best-fit transit and RV models are shown in Figure 7. We list the resulting fitted parameters in Table 5 along with several derived physical parameters.

3.3. Stellar Rotation and Activity

TESS PDC SAP photometry is not always suitable for stellar variability studies, as the stellar variability can be removed by the PDC analysis. To search for rotational spot modulation in the *TESS* photometry, we used the lightkurve package (Barentsen et al. 2019) to produce systematics-corrected light curves from the *TESS* pixel data. The lightkurve package implements a flavor of pixel-level decorrelation (PLD; Deming et al. 2015) to account for the correlated noise induced by the coupling of pointing jitter and intrapixel gain inhomogeneities in the detector. We rejected outliers and normalized the PLD-corrected light curve from each *TESS* Sector to its median flux value, then further binned the data to a one-day cadence for computational efficiency. We elected to analyze Sectors 1–5 and 7–13 independently because of the absence of data from Sector 6, which yielded two nearly evenly sampled data sets. We computed the GLS periodogram (Zechmeister & Kürster 2009) for each of the two data subsets, and found a clear peak in power at ∼24 days in both; less significant peaks can be seen at ∼40 and 55–60 days. Following Livingston et al. (2018), we also computed the ACF of each data subset, after linearly extrapolating the data to a uniformly spaced grid. For both data subsets, the ACF exhibits a higher peak at ∼48 days, which suggests that the ∼24 day signal is the first harmonic of the rotation period (see Figure 8); we concluded that the true stellar rotation period is ∼48 days. To estimate the uncertainty, we also modeled the full binned *TESS* time series as a Gaussian Process (Rasmussen & Williams 2005) with a quasi-periodic kernel, which enabled us to sample the posterior distribution via MCMC; we found the rotation period to be 47.8 ± 0.7 days.

LHS 1815 was also observed by WASP-South over the period of 2008–2012 for a typical duration of 150 days in each year. WASP-South is an array of eight cameras combining 200 mm $f/1.8$ lenses with $2k \times 2k$ CCDs and observing with a broadband filter giving a 400–700 nm bandpass (Pollacco et al. 2006). Each visible field was monitored with a cadence of ∼15 minutes on every clear night, accumulating 50,000 data points on LHS 1815. The light curves from each observing season were searched for rotational modulations using the methods described in Maxted et al. (2011). For LHS 1815, we found a persistent modulation with a period of 24.9 ± 1.1 days with an amplitude of 2–8 mmag (Figure 9) and an FAP below 1%. This is consistent with the signal found in the *TESS* data, and confirms that the signal is likely caused by rotation as it is persistent for multiple years. Future *TESS* data to be obtained during the *TESS* Extended Mission will allow better identification of the correct rotation period of this target.

To assess stellar activity levels spectroscopically, we also extracted the chromatic index (CRX) and differential line width (dLW) indicators from the HARPS spectra using the publicly available SpEctrum Radial Velocity AnaLyser pipeline (SERVAL; Zechmeister et al. 2018). CRX summarizes the wavelength dependence of the RVs, and dLW is an alternative to the commonly used FWHM. The apparent lack of a significant correlation between the activity indicators and the RVs suggests that the RVs are not dominated by stellar activity (see Figure 10). The observed RV scatter is therefore likely caused primarily by the Doppler signal induced by the planet, consistent with the detection of a peak in the GLS periodogram at the frequency of the orbital period (Figure 3).

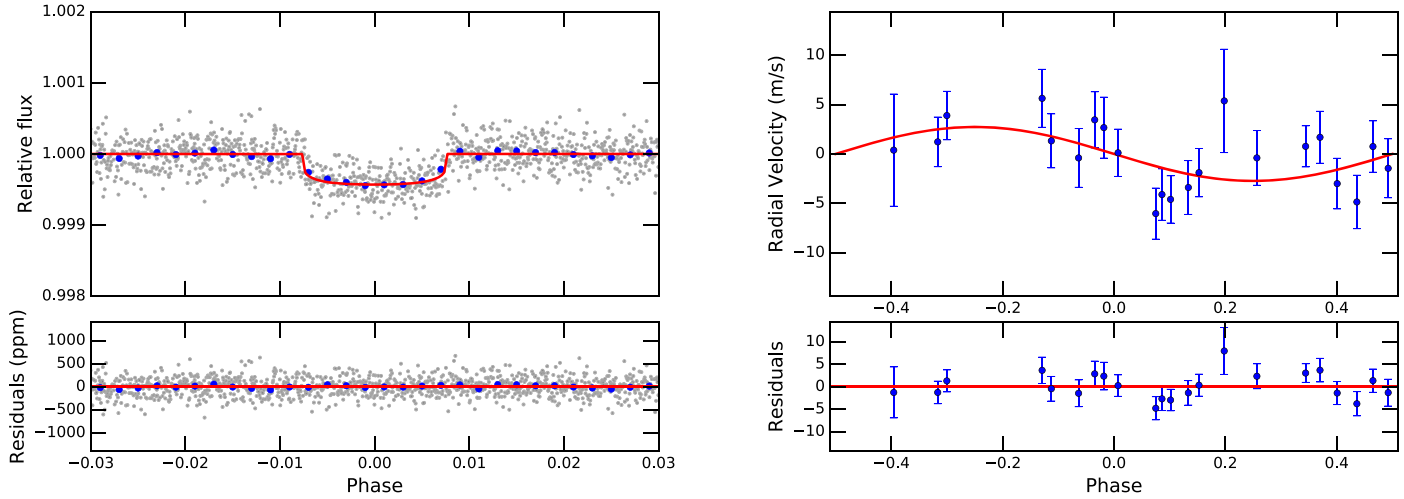

Figure 7. Left: phase-folded and normalized *TESS* photometric data. Binned light curves with different bin size are plotted with gray and blue points, respectively. Best-fit transit model is shown as a red solid line. Residuals are plotted below. Right: phase-folded RV curve of LHS 1815. Blue points represent RVs extracted from the HARPS spectra with the TERRA pipeline. Error bars are the quadrature sum of the instrument jitter term and the measurement uncertainties for all RVs. Best-fit model is shown as a red solid line. Residuals are shown below.

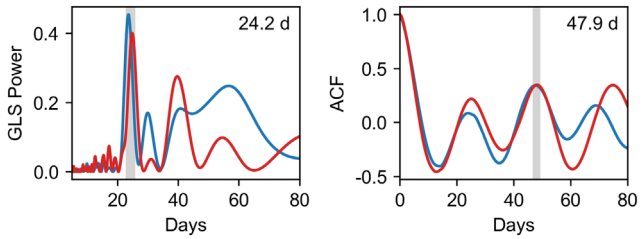

Figure 8. GLS power spectrum (left) and ACF (right) of the PLD-corrected *TESS* photometry from Sectors 1–5 (blue) and 7–13 (red), with the peaks indicated by gray vertical shading. Mean values of the period from each data subset are annotated in the upper right.

3.4. False Positive Analysis

As we previously discussed in Section 2.2, there are several scenarios which can cause a false positive—a transit-like signal in the *TESS* data that does not originate from a transiting star–planet system. We considered all data we have obtained and carefully ruled out the false-positive scenarios below following Vanderspek et al. (2019), Crossfield et al. (2019), and Shporer et al. (2020).

1. *Detection is caused by instrumental artifact*:

We excluded this possibility because periodic transit signals were found in all 12 *TESS* sectors in which this target was observed, and in each sector the target was located at different CCD position.

2. *LHS 1815 is a stellar eclipsing binary*:

Our HARPS RV data did not show a significant RV variability at the few m s^{-1} level. The 3σ mass upper limit has also ruled out this scenario (Section 3.2).

3. *Light from an NEB is blended with LHS 1815*:

Our two ground-based observations from LCO have cleared all nearby *Gaia* stars ($\Delta T \sim 8.7$ mag) within 2.″5 through the NEB analysis (Section 2.2). We did not find any obvious variation of those stars, which indicates this cannot be the case. We have also made sure that the scatter in light curves of nearby stars is smaller than the expected eclipse depth given the brightness difference between the nearby star and the target.

4. *Light from an unassociated distant eclipsing binary or a transiting planet system fully blended with LHS 1815*:

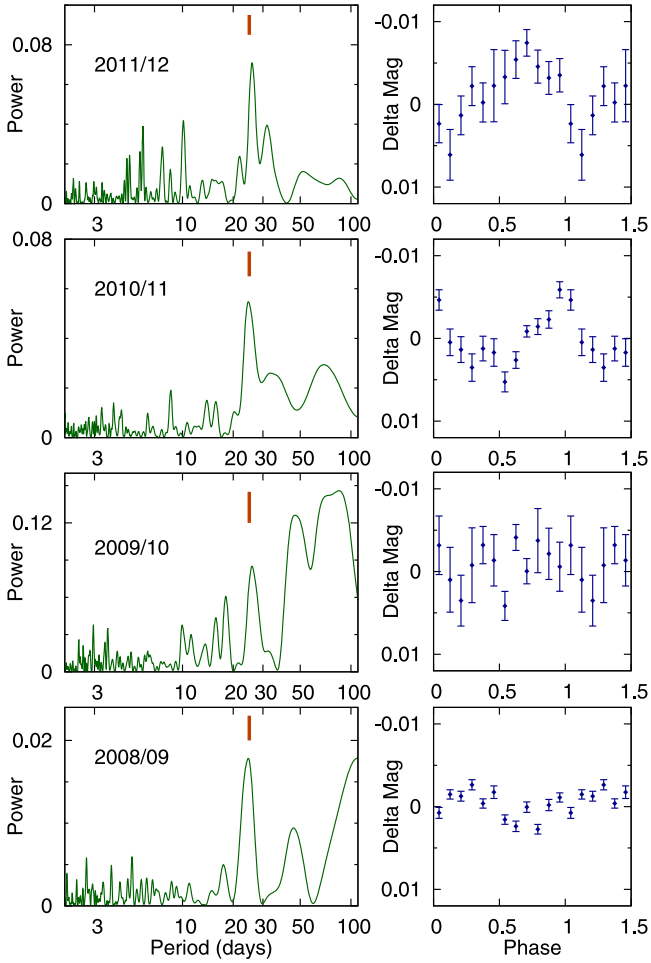

Figure 9. Periodograms of the WASP-South data in each observing season, along with (right) folds of the data on the 24.9 days modulation (marked by orange ticks).

Thanks to the high proper motion of LHS 1815 ($\sim$760 mas yr^{-1}), we can easily reject this scenario by checking images from other surveys decades ago. We did not see any other stars that are bright enough to cause the transit seen in

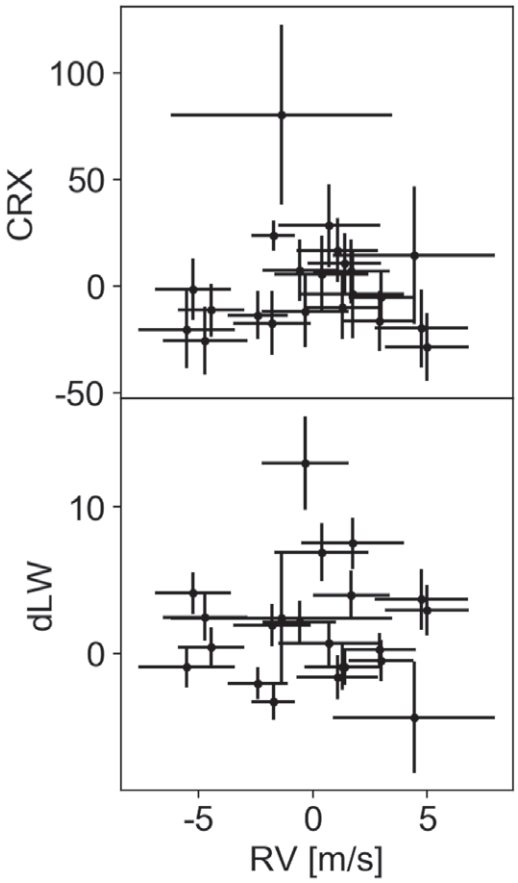

Figure 10. CRX and dLW as a function of RV extracted from the HARPS spectra by the SERVAL pipeline.

TESS data at the current position of LHS 1815, as shown in Figure 2, and thus this possibility is excluded.

5. *LHS 1815 has a stellar binary companion on a wide orbit and that binary companion is the origin of the transit signal*:

Photometric data from multiple sectors of *TESS* offered us an opportunity to deliver precise duration of transit ingress/egress and the time from first-to-third contact during the transit event. Assuming a symmetric light curve, we have

$$\frac{\tau_{12}}{\tau_{13}} = \frac{t_{\rm T} - t_{\rm F}}{t_{\rm T} + t_{\rm F}}, \tag{1}$$

where $t_{\rm T}$ and $t_{\rm F}$ are the total and in-transit duration (second to third contacts), respectively. Seager & Mallén-Ornelas (2003) gave the upper limit of the radius ratio of the transiting planet:

$$\frac{R_{\rm p\_real}}{R_\star} \leqslant \frac{\tau_{12}}{\tau_{13}}. \tag{2}$$

We constrained the relative flux drop if the signal is from an unresolved star:

$$\frac{\Delta F}{f_{\rm b}} = \left(\frac{R_{\rm p\_real}}{R_\star}\right)^2 \leqslant \left(\frac{\tau_{12}}{\tau_{13}}\right)^2 = 0.06\%. \tag{3}$$

Given the 3σ lower limit on the exact transit depth from global modeling, the blended star has to contribute at least 50% of the total flux in the *TESS* aperture:

$$\frac{\Delta F}{f_{\rm s} + f_{\rm b}} \geqslant 0.03\%; \tag{4}$$

$$\frac{f_b}{f_s + f_b} \geqslant 50\%, \tag{5}$$

where f_s and f_b are the source flux and blending flux. We excluded this scenario mainly based on the following reasons:

(1) According to this scenario, the blending star is expected to have >50% contribution to the *TESS* flux, but *Gaia* and high resolution images show a nondetection of a nearby star at a few arcsec from the target.
(2) A star that is comparable in brightness to the target would make the spectrum appear double-lined, but we do not see this phenomenon in the spectrum from HARPS.
(3) A star that is comparable in brightness to the target would cause the target to appear brighter for its distance. Since the distance is given by the *Gaia* DR2 parallax and $T_{\rm eff}$ is constrained by the SED, a blended star with comparable brightness will make the target appear too bright given its distance for a main-sequence star, which is not the case.

4. Constraints from Tidal Evolution

We estimated the timescales for circularization and tidal decay using the equilibrium tide model from Hut (1981). We integrated the secularly averaged equations for the eccentricity and semimajor axis of the planet—namely, Equations (9) and (10) from Hut (1981)—using the midpoint method. We neglected the evolution of the planetary spin, since the spin angular momentum of the planet is too small with respect to the orbital angular momentum to affect the orbit significantly. Given the upper limit estimate for the mass $M_{\rm P}$ of LHS 1815b and the intrinsic uncertainty of tidal efficiency parameters (the time-lag τ or the tidal quality factor Q'), we have explored different tidal evolution models in the range $10\,{\rm s} < \tau < 1000\,{\rm s}$ and $1\,M_\oplus < M_{\rm P} < 6\,M_\oplus$. This range of time lag is appropriate for planets with rocky composition (Socrates et al. 2012). For low tidal efficiency ($\tau = 10$ s), circularization takes longer than 10 Gyr regardless of the mass of the planet, while for high tidal efficiency ($\tau = 1000$ s), the planetary orbit is always completely circularized within 10 Gyr, with small planetary masses ($M_{\rm P} < 3\,M_\oplus$) circularizing within 1 Gyr. On the other hand, at moderate tidal efficiency ($\tau = 100$ s), the circularization timescale is sensible to the planetary mass. For $\tau = 100$ s and $M_{\rm P} < 3\,M_\oplus$, the planetary orbit reaches $e \lesssim 0.05$ within 10 Gyr, while it retains some eccentricity for higher planetary masses ($M_{\rm P} > 3\,M_\oplus$).

Figure 11 shows the evolution of orbital period and eccentricity of the planet, assuming $M_{\rm P} = 4.5\,M_\oplus$, a constant time lag of $\tau = 300$ s, and an apsidal constant of $k_A = 0.3$, corresponding to a tidal quality factor of $Q' = 5 \times 10^2$. In the top panel of Figure 11, the planet has an initial period equal to the currently observed one, and different initial eccentricities. Initial eccentricities lower than 0.5 will be dissipated within about 5 Gyr, the lower the eccentricity, the longer the circularization time. However, as the eccentricity is dissipated, the orbital period decays so that the final period does not match the observed one. Specifically, the orbital period would mismatch the observed one within 100–200 Myr for all eccentricities $e \gtrsim 0.05$.

In the bottom panel of Figure 11, we show the evolution for different initial periods so that the final period after circularization matches the present one. By 5 Gyr, all the

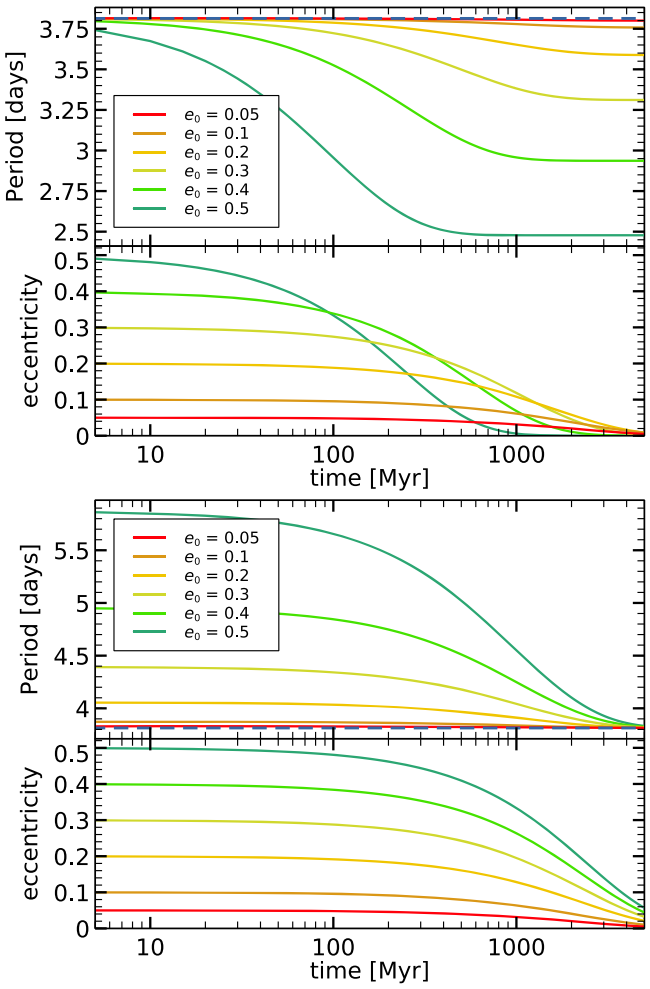

Figure 11. Period and eccentricity as a function of time for different initial eccentricities. Blue dashed line indicates the 5σ error on the inferred period, which is smaller than the thickness of the line. Top panel: starting period equal to the observed one. Bottom panel: initial period chosen so that the final period after circularization matches the observed one.

periods have reached the final value of 3.81433 days with $e \lesssim 0.05$. If the system was younger than 5 Gyr, it would not have time to circularize unless the initial eccentricity was $e \lesssim 0.1$. Alternatively, it might be argued that the planet has not circularized yet. However, as shown by the top panel of Figure 11, any residual eccentricity higher than 0.05 at 3.81433 days would make the planet decay within 100 Myr.

Ultimately, constraints on the age of the system would help to narrow down the possible range of eccentricities of the planet. If the system is very young (~100 Myr), the eccentricity is largely uncertain because the planet must be currently undergoing tidal circularization. Conversely, if the system is old (>5 Gyr), tidal circularization is mostly over and the eccentricity at present day is likely less than 0.05. Note also that the eccentricity could be excited by another undetected planet, a possibility that we have neglected in our analysis.

5. Thick-disk Characteristics

We confirmed the thick-disk nature of LHS 1815 mainly on the basis of its kinematic information. In general, thick-disk stars are kinematically hotter (larger velocity dispersions) than stars that belong to the thin disk. We converted radial velocities and proper motions from *Gaia* DR2 to 3D velocities U, V, and W[39] using the distance of $d = 29.87 \pm 0.02$ pc from our SED fit based on the method described in Johnson & Soderblom (1987). To relate the space velocities to the local standard of rest (LSR), we adopted solar velocity components relative to the LSR $(U_\odot, V_\odot, W_\odot) = (9.58, 10.52, 7.01)$ km s^{-1} obtained by the Large Sky Area Multi-Object Fiber Spectroscopic Telescope (LAMOST; Tian et al. 2015). We determined the three-dimensional Galactic space motion of $(U_{\rm LSR}, V_{\rm LSR}, W_{\rm LSR}) = (-34.34 \pm 0.04, -71.47 \pm 0.22, 76.26 \pm 0.14)$ km s^{-1}.

To judge which stellar component LHS 1815 belongs to, we employed the kinematical criteria first mentioned in Bensby et al. (2003) by assuming the Galactic space velocities $U_{\rm LSR}$, $V_{\rm LSR}$, and $W_{\rm LSR}$ of the stellar populations have Gaussian distributions:

$$f = k \times \exp\left(-\frac{U_{\rm LSR}^2}{2\sigma_U^2} - \frac{(V_{\rm LSR} - V_{\rm asym})^2}{2\sigma_V^2} - \frac{W_{\rm LSR}^2}{2\sigma_W^2}\right), \quad (6)$$

where

$$k = \frac{1}{(2\pi)^{3/2}\sigma_U \sigma_V \sigma_W} \quad (7)$$

is a normalization constant, σ_U, σ_V, and σ_W represent velocity dispersion for 3D velocity components while $V_{\rm asym}$ is the asymmetric drift. We applied related parameters from Bensby et al. (2014) for solar-neighborhood stars and calculated relative probability $P_{\rm thick}/P_{\rm thin}$ for LHS 1815 and other *TESS* planet host stars to be in the thick (TD) and thin disks (D). Figure 12 shows the corresponding Toomre plot. We considered stars with $P_{\rm thick}/P_{\rm thin} > 10$ to be in the thick disk while stars in between $(0.1 < P_{\rm thick}/P_{\rm thin} < 10)$ are ambiguous to judge. Up to now, *TESS* has detected five planet host stars located in the in-between region: TOI 118 (Esposito et al. 2019), TOI 144 (Huang et al. 2018a), TOI 172 (Rodriguez et al. 2019), TOI 186 (Dragomir et al. 2019; Trifonov et al. 2019), and TOI 197 (Huber et al. 2019). Table 4 lists their relative probabilities and none of them show clear-cut thick-disk probability. However, we obtained a large relative probability ($P_{\rm thick}/P_{\rm thin} = 6482$) for LHS 1815, indicating it is very likely a thick-disk star. Soubiran et al. (2003) showed that thick-disk stars tend to have much lower metallicity than thin-disk stars. Therefore, our metallicity measurement [Fe/H] $= -0.12 \pm 0.09$, based on the HARPS spectra, is consistent with a thick-disk origin.

In order to gain insight into further dynamical information, we used galpy (Bovy 2015) to simulate the orbit of LHS 1815. We initialized the orbit using R.A., decl., star distance, proper motions in two directions and heliocentric line-of-sight velocity. We integrated the orbit from $t = 0$ to $t = 10$ Gyr in a general potential: MWPotential2014, saving the orbit for 10,000 steps. The orbital result of LHS 1815 is shown in Figure 13. The maximal height $Z_{\rm max}$ of LHS 1815 above the plane of the orbit is 1.8 kpc, consistent with our thick disk conclusion before. For comparison, we plot $Z_{\rm max}$ and the relative probability of all *TESS* planet host stars in Figure 14, which are listed in Table 4. It is clear that the five TOI stars located in the region between the thin and thick disks are more likely to belong to the Galactic thin disk given their small $Z_{\rm max}$.

[39] U, V, and W are positive in the directions of Galactic center, Galactic rotation, and the North Galactic Pole.

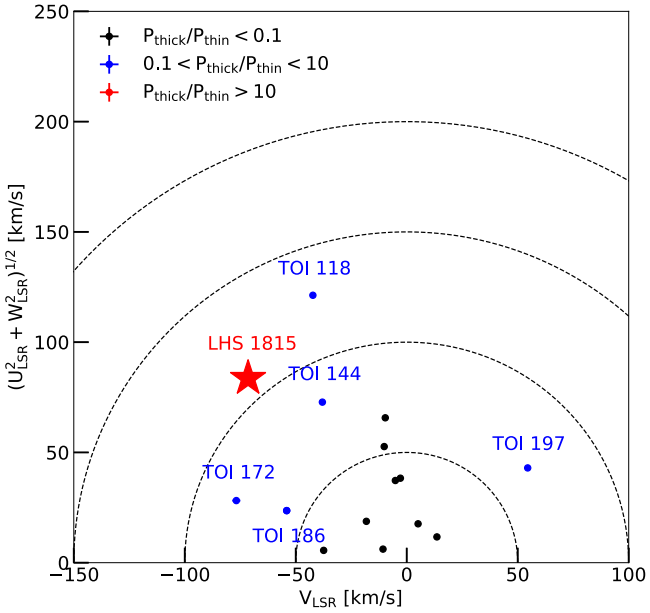

Figure 12. Toomre plot for all *TESS* host stars with planets. Different color represent different ranges of relative probability. Our target is shown as a red star.

Table 4
Relative Probability for *TESS* Stars with Ambiguous Separation Between Thick and Thin Components

Star	$P_{\rm thick}/P_{\rm thin}$
TOI-118	4.825
TOI-144	0.127
TOI-172	1.430
TOI-186	0.125
TOI-197	0.292
LHS 1815	6482

LHS 1815 is currently moving upward; an additional orbital integration analysis shows that LHS 1815 will spend ∼14 Myr to first reach 1 kpc above the Galactic plane. Before LHS 1815 reaches the plane again, we have a probability of about 33% to see it ($Z < 1$ kpc).

6. Discussion and Conclusion

LHS 1815b is the first thick-disk planet detected by *TESS*. It has a radius of $R_P = 1.088 \pm 0.064\,R_\oplus$ and a mass of $M_{\rm P} = 4.2 \pm 1.5\,M_\oplus$. The proximity of LHS 1815 and its interesting kinematic features make it a system worthy of further characterization.

6.1. Prospects on Future Follow-up Observations

Given the brightness of LHS 1815, it is an attractive target for precise RV measurements with high-resolution spectroscopy facilities. Those will lead to precise mass measurement of the transiting planet and will be used to search for other planets in the system. A precise planet mass will give an improved estimate of the suitability of LHS 1815b for atmospheric characterization. The rotation period of LHS 1815 is well-separated from the orbital period of the planet, making it possible to smooth out the effect from stellar activity.

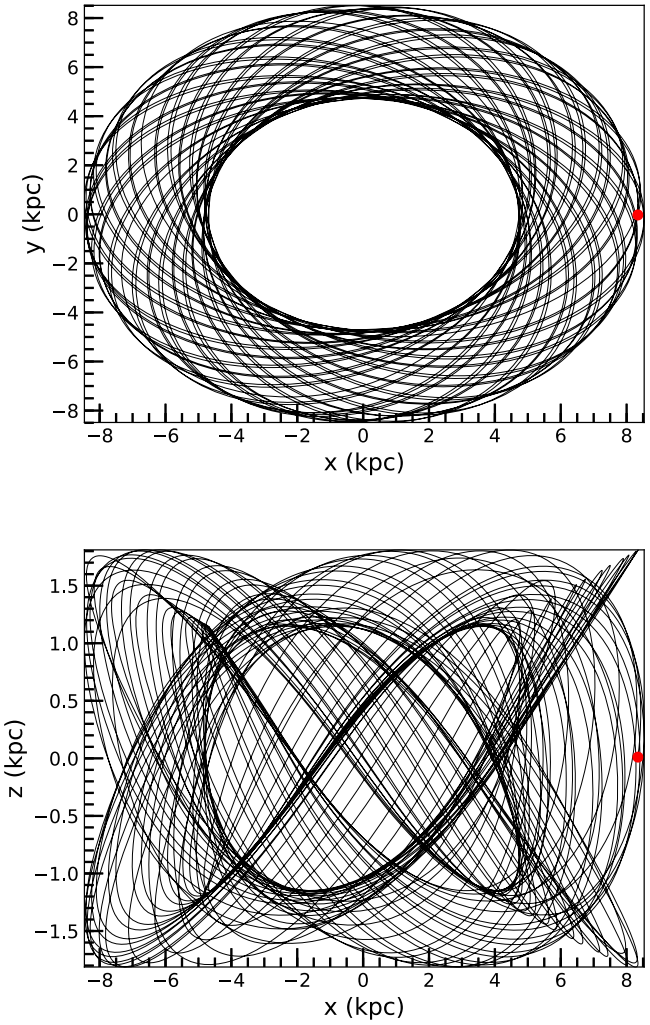

Figure 13. Top panel: orbit of LHS 1815 in the Galactic potential MWPotential2014 obtained using galpy (Bovy 2015) in the top-down view. Bottom panel: same orbit but viewed edge-on. Red dots represent the present position of the star.

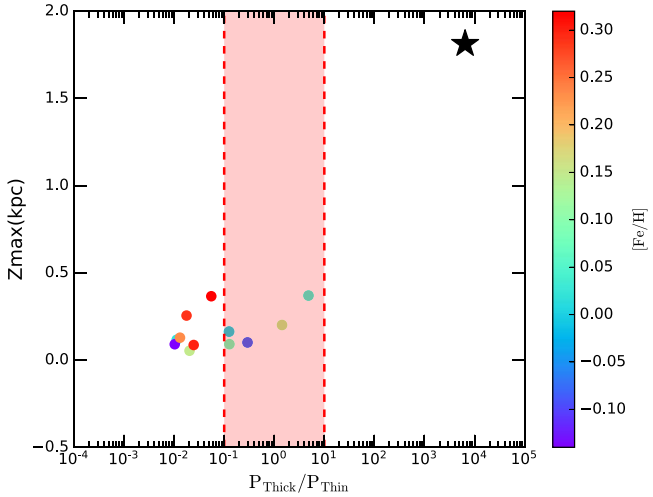

Figure 14. The $Z_{\rm max}$ vs. relative probability $P_{\rm thick}/P_{\rm thin}$ for all *TESS* planet host stars with *Gaia* RV. Here, $Z_{\rm max}$ is the expected maximal height of stars above the Galactic plane. Different colors represent different metallicities. Red vertical dashed lines mean relative probability = 0.1 and 10. LHS 1815 is marked as a black star at the top right.

Table 5
Final Parameters of LHS 1815b

Parameter	Value	Prior
Fitting parameters		
$P_{\rm orb}$ (days)	3.81433 ± 0.00003	$\mathcal{N}$[a] (3.814, 0.1^2)
$T_{\rm C}$ (BJD)	$2458{,}327.4161 \pm 0.0016$	$\mathcal{N}$ (2458,327.4, 0.1)
$R_{\rm P}/R_\star$	0.0199 ± 0.0009	$\mathcal{U}$[b] (0.005, 0.05)
$a/R_\star$	17.403 ± 2.816	$\mathcal{N}$ (16, 3)
i (deg)	88.125 ± 1.113	$\mathcal{U}$ (0, 180)
q_1	0.26 ± 0.19	$\mathcal{U}$ (0, 1)
q_2	0.35 ± 0.26	$\mathcal{U}$ (0, 1)
K (m s^{-1})	2.7 ± 1.0	$\mathcal{U}$ (0, 10)
$\gamma_{\rm rel}$ (m s^{-1})	-0.38 ± 0.64	$\mathcal{U}$ (−10, 10)
$\sigma_{\rm J}$ (m s^{-1})	2.0 ± 0.6	$\mathcal{J}$[c] (0.1, 10)
e	0	Fixed
ω (deg)	90	Fixed
Derived parameters		
$R_{\rm P}$ ($R_\oplus$)	1.088 ± 0.064	
$M_{\rm P}$ ($M_\oplus$)[d]	4.2 ± 1.5	
a (au)	0.0404 ± 0.0094	
$T_{\rm eq}$ (K)[e]	617 ± 84	

Notes.
[a] $\mathcal{N}(\mu, \sigma)$ means a normal prior with mean μ and standard deviation σ.
[b] $\mathcal{U}(a, b)$ stands for a uniform prior ranging from a to b.
[c] $\mathcal{J}(a, b)$ stands for a Jeffrey's prior with the same limits.
[d] This is not a statistically significant measurement. The 3σ mass upper-limit is 8.7 $M_\oplus$.
[e] Suppose albedo = 0 and there is no heat distribution here.

In addition, because LHS 1815 is nearby (29.87 ± 0.02 pc), future release of *Gaia* time series astrometry can be used to look for massive objects (massive planets and brown dwarfs) at wide orbits, with potential partial overlap with objects on orbits that radial velocities will be sensitive to.

To evaluate the feasibility of high-quality atmospheric characterization by *JWST* (Gardner et al. 2006), we first use the Transmission Spectroscopy Metric (TSM) formulated by Kempton et al. (2018) and we find TSM $\sim 2.5^{+3.8}_{-1.3}$ for LHS 1815. Kempton et al. (2018) posits that planets with TSM > 10 for $R_{\rm p} < 1.5\,R_\oplus$ are high-quality atmospheric characterization targets. The relatively large TSM uncertainty due to the weak constraint on the planet mass results in unclear determination on whether LHS 1815 is a good (although unlikely the best) target for transmission spectroscopy studies. In addition, we compute the Emission Spectroscopy Metric (ESM) for LHS 1815 and we find ESM $\sim 1.9^{+1.0}_{-0.8}$. Given the recommended threshold ESM = 7.5 from Kempton et al. (2018), LHS 1815 is not an ideal target for emission spectroscopy researches, either.

6.2. Planet Formation Efficiency in Thin and Thick Disks?

Follow-up statistical work about planet formation efficiency in the thin and thick disk is ongoing (T. Gan et al. 2020, in preparation), based on all *TESS* planet candidates detected in the Southern Hemisphere. The current *TESS* survey for the Northern Hemisphere will be an excellent opportunity to further examine this subject. First, *TESS* focuses on finding exoplanets around nearby bright stars. Most TOIs have precise astrometry and RV measurement from *Gaia* DR2, which can determine their thin, thick, and halo origin. Second, LAMOST (Cui et al. 2012) can provide chemical element abundance measurements to check the classification for a large number of stars.

We emphasize that here we only consider the formation efficiency for nearby bright stars. Faint stars ($G > 13$ mag) at relatively large distances may not have RV measurement from *Gaia* DR2, leading to a poor separation between thin and thick disks. Future surveys such as DESI (DESI Collaboration et al. 2016) and spectroscopic observations from SPIRou (Challita et al. 2018) shall remedy this situation.

We thank Sharon Xuesong Wang, Chao Liu, and Weicheng Zang for their insights and advice. Funding for the *TESS* mission is provided by NASA's Science Mission directorate. This work is partly supported by the National Science Foundation of China (grant No. 11390372 and 11761131004 to S.M. and G.T.J.). We acknowledge the use of *TESS* Alert data from pipelines at the *TESS* Science Office and at the *TESS* Science Processing Operations Center. Resources supporting this work were provided by the NASA High-End Computing (HEC) Program through the NASA Advanced Supercomputing (NAS) Division at Ames Research Center for the production of the SPOC data products. J.G.W. is supported by a grant from the John Templeton Foundation. The opinions expressed in this publication are those of the authors and do not necessarily reflect the views of the John Templeton Foundation. A.A.T. acknowledges support from JSPS KAKENHI Grant Number 17F17764 and 17H06360. C.Z. is supported by a Dunlap Fellowship at the Dunlap Institute for Astronomy & Astrophysics, funded through an endowment established by the Dunlap family and the University of Toronto. Some of the observations in the paper made use of the High-Resolution Imaging instrument Zorro at Gemini-South). Zorro was funded by the NASA Exoplanet Exploration Program and built at the NASA Ames Research Center by Steve B. Howell, Nic Scott, Elliott P. Horch, and Emmett Quigley. This research has made use of the Exoplanet Follow-up Observation Program website, which is operated by the California Institute of Technology, under contract with the National Aeronautics and Space Administration under the Exoplanet Exploration Program. This paper includes data collected by the *TESS* mission, which are publicly available from the Mikulski Archive for Space Telescopes (MAST). This research made use of observations from the LCO network, WASP-South and ESO: 3.6m (HARPS). N. A.-D. acknowledges the support of FONDECYT project 3180063. B.R-A acknowledges the funding support from FONDECYT through grant 11181295.

Facilities: TESS, ESO 3.6 m: HARPS, 4.1-m Southern Astrophysical Research (SOAR), Gemini-South, LCO:1.0m (Sinistro), WASP-south, *Gaia*.

Software: AstroImageJ (Collins et al. 2017), TERRA (Anglada-Escudé & Butler 2012), SERVAL (Zechmeister et al. 2018), SpecMatch-Emp (Yee et al. 2017), lightkurve (Barentsen et al. 2019), EXONAIER (Espinoza et al. 2016), batman (Kreidberg 2015), radvel (Fulton et al. 2018), emcee (Foreman-Mackey et al. 2013).

ORCID iDs

Tianjun Gan https://orcid.org/0000-0002-4503-9705
Avi Shporer https://orcid.org/0000-0002-1836-3120
John H. Livingston https://orcid.org/0000-0002-4881-3620
Karen A. Collins https://orcid.org/0000-0001-6588-9574
Shude Mao https://orcid.org/0000-0001-8317-2788

Alessandro A. Trani https://orcid.org/0000-0001-5371-3432
Davide Gandolfi https://orcid.org/0000-0001-8627-9628
Teruyuki Hirano https://orcid.org/0000-0003-3618-7535
Rafael Luque https://orcid.org/0000-0002-4671-2957
Keivan G. Stassun https://orcid.org/0000-0002-3481-9052
Carl Ziegler https://orcid.org/0000-0002-0619-7639
Steve B. Howell https://orcid.org/0000-0002-2532-2853
Coel Hellier https://orcid.org/0000-0002-3439-1439
David R. Anderson https://orcid.org/0000-0001-7416-7522
Nicholas Law https://orcid.org/0000-0001-9380-6457
Andrew W. Mann https://orcid.org/0000-0003-3654-1602
Nicola Astudillo-Defru https://orcid.org/0000-0002-8462-515X
Eric L. N. Jensen https://orcid.org/0000-0002-4625-7333
George R. Ricker https://orcid.org/0000-0003-2058-6662
Roland Vanderspek https://orcid.org/0000-0001-6763-6562
David W. Latham https://orcid.org/0000-0001-9911-7388
Sara Seager https://orcid.org/0000-0002-6892-6948
Joshua N. Winn https://orcid.org/0000-0002-4265-047X
Jon M. Jenkins https://orcid.org/0000-0002-4715-9460
Natalia M. Guerrero https://orcid.org/0000-0002-5169-9427
Elisa Quintana https://orcid.org/0000-0003-1309-2904
Joseph D. Twicken https://orcid.org/0000-0002-6778-7552
Chelsea X. Huang https://orcid.org/0000-0003-0918-7484
Pamela Rowden https://orcid.org/0000-0002-4829-7101
Bárbara Rojas-Ayala https://orcid.org/0000-0002-0149-1302

References

Adibekyan, V. Z., Figueira, P., Santos, N. C., et al. 2013, A&A, 554, A44
Adibekyan, V. Z., Santos, N. C., Sousa, S. G., & Israelian, G. 2011, A&A, 535, L11
Anglada-Escudé, G., & Butler, R. P. 2012, ApJS, 200, 15
Baglin, A., Auvergne, M., Barge, P., et al. 2006, ESASP, 1306, 33
Bakos, G., Noyes, R. W., Kovács, G., et al. 2004, PASP, 116, 266
Barentsen, G., Hedges, C., Vinícius, Z., et al. 2019, KeplerGO/lightkurve: Lightkurve v1.0b29, Zenodo, doi:10.5281/zenodo.2565212
Bensby, T., Feltzing, S., & Lundström, I. 2003, A&A, 410, 527
Bensby, T., Feltzing, S., Lundström, I., & Ilyin, I. 2005, A&A, 433, 185
Bensby, T., Feltzing, S., & Oey, M. S. 2014, A&A, 562, A71
Borucki, W. J., Koch, D., Basri, G., et al. 2010, Sci, 327, 977
Bouchy, F., Hebb, L., Skillen, I., et al. 2010, A&A, 519, A98
Bovy, J. 2015, ApJS, 216, 29
Brown, T. M. 2003, ApJL, 593, L125
Brown, T. M., Baliber, N., Bianco, F. B., et al. 2013, PASP, 125, 1031
Buser, R., Rong, J., & Karaali, S. 1999, A&A, 348, 98
Campante, T. L., Barclay, T., Swift, J. J., et al. 2015, ApJ, 799, 170
Challita, Z., Reshetov, V., Baratchart, S., et al. 2018, Proc. SPIE, 10702, 1070262
Claret, A. 2018, A&A, 618, A20
Collins, K. A., Kielkopf, J. F., Stassun, K. G., & Hessman, F. V. 2017, AJ, 153, 77
Crossfield, I. J. M., Waalkes, W., Newton, E. R., et al. 2019, ApJL, 883, L16
Cui, X.-Q., Zhao, Y.-H., Chu, Y.-Q., et al. 2012, RAA, 12, 1197
Cutri, R. M., Skrutskie, M. F., van Dyk, S., et al. 2003, yCat, II/246, 0
Deeg, H. J., Gillon, M., Shporer, A., et al. 2009, A&A, 506, 343
Deming, D., Knutson, H., Kammer, J., et al. 2015, ApJ, 805, 132
DESI Collaboration, Aghamousa, A., Aguilar, J., et al. 2016, arXiv:1611.00036
Dragomir, D., Teske, J., Günther, M. N., et al. 2019, ApJL, 875, L7
Espinoza, N., Brahm, R., Jordán, A., et al. 2016, ApJ, 830, 43
Esposito, M., Armstrong, D. J., Gandolfi, D., et al. 2019, A&A, 623, A165
Foreman-Mackey, D., Hogg, D. W., Lang, D., & Goodman, J. 2013, PASP, 125, 306
Fuhrmann, K. 2008, MNRAS, 384, 173
Fuhrmann, K., & Bernkopf, J. 2008, MNRAS, 384, 1563
Fulton, B. J., Petigura, E. A., Blunt, S., & Sinukoff, E. 2018, PASP, 130, 044504
Gaia Collaboration, Babusiaux, C., van Leeuwen, F., et al. 2018, A&A, 616, A10
Gardner, J. P., Mather, J. C., Clampin, M., et al. 2006, SSRv, 123, 485
Gilmore, G., & Reid, N. 1983, MNRAS, 202, 1025
Gonzalez, G. 1997, MNRAS, 285, 403
Hippke, M., & Heller, R. 2019, A&A, 623, A39
Hirano, T., Dai, F., Livingston, J. H., et al. 2018, AJ, 155, 124
Howell, S. B., Everett, M. E., Sherry, W., Horch, E., & Ciardi, D. R. 2011, AJ, 142, 19
Howell, S. B., Sobeck, C., Haas, M., et al. 2014, PASP, 126, 398
Huang, C. X., Burt, J., Vanderburg, A., et al. 2018a, ApJL, 868, L39
Huang, C. X., Shporer, A., Dragomir, D., et al. 2018b, arXiv:1807.11129
Huber, D., Chaplin, W. J., Chontos, A., et al. 2019, AJ, 157, 245
Hut, P. 1981, A&A, 99, 126
Jenkins, J. M. 2002, ApJ, 575, 493
Jenkins, J. M., Tenenbaum, P., Seader, S., et al. 2017, Kepler Data Processing Handbook: Transiting Planet Search, Kepler Science Document, KSCI-19081-002
Jenkins, J. M., Twicken, J. D., McCauliff, S., et al. 2016, Proc. SPIE, 9913, 99133E
Johnson, D. R. H., & Soderblom, D. R. 1987, AJ, 93, 864
Jurić, M., Ivezić, Ž, Brooks, A., et al. 2008, ApJ, 673, 864
Kempton, E. M. R., Bean, J. L., Louie, D. R., et al. 2018, PASP, 130, 114401
Kreidberg, L. 2015, PASP, 127, 1161
Livingston, J. H., Dai, F., Hirano, T., et al. 2018, AJ, 155, 115
Mann, A. W., Dupuy, T., Kraus, A. L., et al. 2019, ApJ, 871, 63
Mann, A. W., Feiden, G. A., Gaidos, E., Boyajian, T., & von Braun, K. 2015, ApJ, 804, 64
Maxted, P. F. L., Anderson, D. R., Collier Cameron, A., et al. 2011, PASP, 123, 547
Mayor, M., Pepe, F., Queloz, D., et al. 2003, Msngr, 114, 20
McTier, M. A. S., & Kipping, D. M. 2019, MNRAS, 489, 2505
Mermilliod, J. C. 2006, yCat, II/168, 0
Murdoch, K. A., Hearnshaw, J. B., & Clark, M. 1993, ApJ, 413, 349
Neves, V., Santos, N. C., Sousa, S. G., Correia, A. C. M., & Israelian, G. 2009, A&A, 497, 563
Pecaut, M. J., & Mamajek, E. E. 2013, ApJS, 208, 9
Perger, M., García-Piquer, A., Ribas, I., et al. 2017, A&A, 598, A26
Pollacco, D. L., Skillen, I., Collier Cameron, A., et al. 2006, PASP, 118, 1407
Prochaska, J. X., Naumov, S. O., Carney, B. W., McWilliam, A., & Wolfe, A. M. 2000, AJ, 120, 2513
Rasmussen, C. E., & Williams, C. K. I. 2005, Gaussian Processes for Machine Learning (Adaptive Computation and Machine Learning) (Cambridge, MA: MIT Press)
Reddy, B. E., Lambert, D. L., & Allende Prieto, C. 2006, MNRAS, 367, 1329
Reid, I. N., Turner, E. L., Turnbull, M. C., Mountain, M., & Valenti, J. A. 2007, ApJ, 665, 767
Ricker, G. R., Winn, J. N., Vanderspek, R., et al. 2014, Proc. SPIE, 9143, 914320
Rodriguez, J. E., Quinn, S. N., Huang, C. X., et al. 2019, AJ, 157, 191
Sartoretti, P., Katz, D., Cropper, M., et al. 2018, A&A, 616, A6
Seager, S., & Mallén-Ornelas, G. 2003, ApJ, 585, 1038
Shporer, A., Collins, K. A., Astudillo-Defru, N., et al. 2020, ApJL, 890, L7
Skrutskie, M. F., Cutri, R. M., Stiening, R., et al. 2006, AJ, 131, 1163
Smith, J. C., Stumpe, M. C., Van Cleve, J. E., et al. 2012, PASP, 124, 1000
Socrates, A., Katz, B., & Dong, S. 2012, arXiv:1209.5724
Soubiran, C., Bienaymé, O., & Siebert, A. 2003, A&A, 398, 141
Sozzetti, A., Torres, G., Charbonneau, D., et al. 2007, ApJ, 664, 1190
Stassun, K. G., Collins, K. A., & Gaudi, B. S. 2017, AJ, 153, 136
Stassun, K. G., Corsaro, E., Pepper, J. A., & Gaudi, B. S. 2018a, AJ, 155, 22
Stassun, K. G., Oelkers, R. J., Paegert, M., et al. 2019, AJ, 158, 138
Stassun, K. G., Oelkers, R. J., Pepper, J., et al. 2018b, AJ, 156, 102
Stassun, K. G., & Torres, G. 2016, AJ, 152, 180
Stassun, K. G., & Torres, G. 2018, ApJ, 862, 61
Stumpe, M. C., Smith, J. C., Catanzarite, J. H., et al. 2014, PASP, 126, 100
Stumpe, M. C., Smith, J. C., Van Cleve, J. E., et al. 2012, PASP, 124, 985
Sullivan, P. W., Winn, J. N., Berta-Thompson, Z. K., et al. 2015, ApJ, 809, 77
Tian, H.-J., Liu, C., Carlin, J. L., et al. 2015, ApJ, 809, 145
Tokovinin, A. 2018, PASP, 130, 035002
Trifonov, T., Rybizki, J., & Kürster, M. 2019, A&A, 622, L7
Vanderspek, R., Huang, C. X., Vanderburg, A., et al. 2019, ApJL, 871, L24
Wright, E. L., Eisenhardt, P. R. M., Mainzer, A. K., et al. 2010, AJ, 140, 1868
Yee, S. W., Petigura, E. A., & von Braun, K. 2017, ApJ, 836, 77
Zechmeister, M., & Kürster, M. 2009, A&A, 496, 577
Zechmeister, M., Reiners, A., Amado, P. J., et al. 2018, A&A, 609, A12